Simulation of tabular mine face advance rates using a simplified fracture zone model

J A L Napier[1] and D F Malan[1]

[1]Department of Mining Engineering, University of Pretoria, South Africa

Abstract The paper describes a method to determine the time-dependent stability of the fracture zone near the edges of tabular excavation layouts when different mining rates and face advance increment lengths are scheduled. Some analytic properties of the proposed time-dependent fracture zone evolution model are presented initially for a simplified mining geometry. The implementation of the model in a general tabular layout setting is described next including a novel scheme to allow for partially fractured elements. The reef plane stress distribution in the fracture zone is solved using a fast marching method that is coupled to a displacement discontinuity solution of the excavation and fracture zone deformations. The numerical scheme is illustrated by considering the extraction of a hypothetical deep-level mining layout. The sensitivity of the results to changes in the mining rate schedule and the face advance step size are discussed. Further extensions to the solution scheme are noted.

Keywords Tabular mining; Mining rate; Face stability; Fast marching method

1. Introduction

One of the key problems in deep level tabular mine design is the scheduling of mine face positions and face advance rates. The scheduling problem is constrained by the available access to the tabular orebody and by the need to prevent unstable rock failure near mining faces. This requirement is of paramount importance when mining personnel are engaged in operations such as face cleaning, drilling and blasting. In a mechanised environment, it is equally necessary to ensure that automated mine equipment is used efficiently and is protected as far as possible from fall of ground losses.

As early as1966, Cook et al[1] described an increase in rockbursts in the South African gold mines if the face advance rate exceeded more than 4 m/month for small abutments and 8 m/month for large abutments. Studies of mining rate were conducted by Malan[2]. It is generally accepted that high stress peaks close to the face may increase the likelihood of violent failure. A continuum viscoplastic model was studied as an approximation of the time dependent nature of the fracture zone. This model illustrated that high mining rates may lead to higher stress peaks close to the stope face. Similar qualitative results were obtained using a viscoplastic discontinuum model (Napier and Malan[3]). The authors demonstrated that that the cumulative fracture length decreases for faster mining rates, leading to an increase in the value of seismic energy released. As a drawback, these preliminary studies only considered two-dimensional models. Regarding coal mining, Linkov[4] noted that in the Kizel coal mines, doubling the rate of coal cutting on the face from 0.27 m/min to 0.54 m/min resulted in a drastic increase in incidence of rockbursting. Nawrocki[5] developed a one-dimensional semi-analytical solution for the time-dependent behavior of a coal seam to investigate the rate of face advance. The analysis indicated that rapid ore extraction produced zones of high stress concentrations close to the longwall face.

The extraction technique that is used in tabular mining is dictated by the deposit depth and by the rock strength of the orebody. Large-scale mechanised operations are often available in comparatively shallow coal mining operations (at depths that are of the order of hundreds of metres) whereas deep level, hard rock platinum and gold mining operations (at depths that can reach four kilometres) may demand labour-intensive drill, blast and cleaning cycles. It is necessary in all cases to determine an appropriate extraction schedule that does not trigger unstable ground conditions. The planning of these operations can be assisted if proposed mining sequences can be evaluated computationally to determine the likely consequences of mining rate variations, selection of the face advance increment and the choice of the geometric configuration of the excavations.

A simple time-dependent limit equilibrium model of the fracture zone extent near the edges of tabular excavations is described in this paper to facilitate this analysis. The model is applicable specifically to planar seam or reef deposits where the excavations are generally hundreds of metres in extent in the

plane of the orebody but where the mining height is limited typically to vary between one and ten metres. This characteristic narrow mining height geometry can be approximated as a crack-like surface where the opposing crack faces (the excavation roof and floor) interpenetrate one another in response to the imposed stress field (Hackett[6], Berry[7], Berry and Sales[8]). The displacement discontinuity boundary element method (DDM - Crouch and Starfield[9], Salamon[10]) is an appropriate computational tool that can be used to solve the relative roof to floor movements.

The main deficiency of this numerical technique is that the simplified crack-like geometry provides a limited depiction of the mining-induced fracture configuration at the excavation edges. The present paper addresses this deficiency by introducing a simplified representation of the time-dependent evolution of the fracture zone extent in the plane of the excavation. An extensive analysis of the properties of the model is given and it is indicated how the model can be incorporated in a general tabular layout. This enhanced facility enables a more realistic investigation of mining rates and face advance increment choices to be carried out. This is illustrated by considering an important problem of contrasting the face advance rate with the size of the face advance increment.

2. Time-dependent limit equilibrium model

Fig. 1 shows a plan view of a particular tabular layout at depth where the coloured regions depict the successive planned mining sequence of a series of panels. The echelon extraction sequence in this case was designed to leave a central dip pillar (the dip direction is from the top to the bottom of the diagram). One of the essential problems in determining the mining sequence is the geometric sizing of the panels and the detailed extraction rate schedule. The narrow excavation height of the reef deposit generally leads to a significant stress concentration ahead of the mining face which leads to ongoing fracturing of the panel edges as indicated in the adjacent photograph in Fig. 1. The fracture zone formation has been studied extensively in deep level gold mines (Adams and Jager[11]). In addition to these observations, monitoring of the movements between the roof and the floor of tabular excavations at fixed points in the mined area has been carried out (Malan[12]). These observations indicate that the relative roof to floor normal component of deformation (termed stope convergence or closure) has a characteristic time-dependent profile that evolves after each face advance increment (face blast). The closure profile shape depends on the host rock strength properties and on the local excavation configuration and mining rate. It is evident that the observed time-dependent stope convergence movements are related to ongoing deformations in the adjacent fracture zone following each mining step and can provide an indirect indication of local mining face stability (Malan[12], Malan et al[13]).

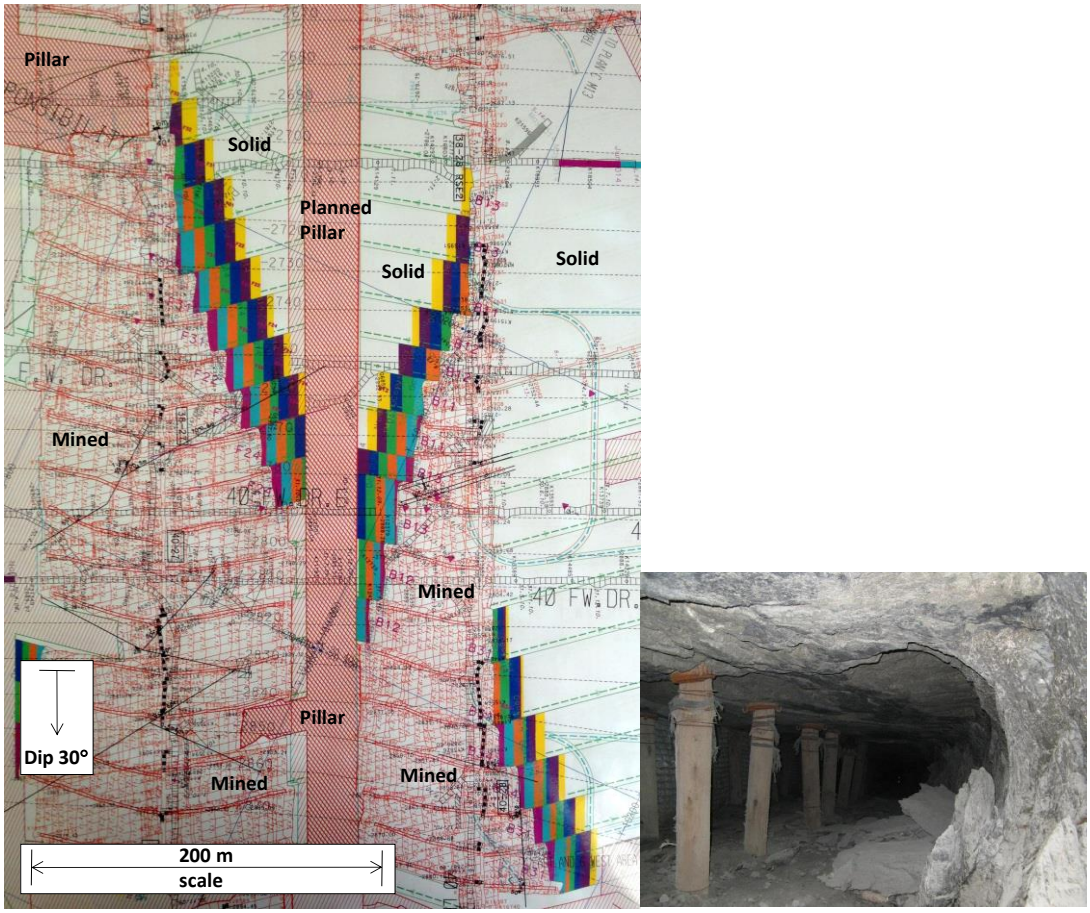

Fig. 1. Plan view of a dip pillar mine layout indicating planned panel extraction sequences. The different colours indicated the planned mining for successive months. The adjacent diagram shows typical conditions in the stope face area of one of the layout panels. The mining face is on the right and the fracturing caused by the stress concentration in this area is evident.

A model of the time-dependent behaviour has been proposed previously by Napier and Malan[14]. The model is based on a simple limit equilibrium representation of the fractured rock and is embedded in a displacement discontinuity representation of the excavation region (Napier and Malan[14]). It is assumed that a zone of crushed rock exists adjacent to the excavation edge, within the plane of the excavation, and that the reef-normal stress distribution in the fracture zone is determined by the reef-parallel confining stress ahead of the excavation edge. Fig. 2 shows a schematic differential force balance within a plane section normal to the reef plane and perpendicular to the local excavation panel edge. The effective height of the fractured material is H and the length of the fracture zone is L. The average reef-parallel confining stress $\sigma_s(x,t)$ at position x and time t is balanced by a frictional shear traction $\mu_I \sigma_n(x,t)$ at the interfaces between the fractured material and the intact rock. μ_I is the

effective interface friction coefficient and $\sigma_n(x,t)$ is the traction component normal to the reef plane. The limit strength model postulates that a specific relationship exists between $\sigma_n(x,t)$ and $\sigma_s(x,t)$ within the fractured material that takes the form

$$\sigma_n(x,t) = \sigma_c(x,t) + m(x,t)\sigma_s(x,t)\,, \tag{1}$$

where the strength envelope parameters $\sigma_c(x,t)$ and $m(x,t)$ are position and time-dependent functions.

This representation of the fractured material constitutive properties is highly simplified but has been considered in the design of coal mine pillar layouts (Barron[15,16]) and is equivalent to a triangular wedge block model proposed for plane strain tabular mining panels by Brummer[17]. A more elaborate two-dimensional section model has been presented by Salamon[18] but this model can be shown to behave similarly to the average stress model treated here. Employing equation (1), it can be deduced from Fig. 2 that the average reef-parallel confining stress $\sigma_s(x,t)$ at position *x* and time *t* must obey the differential force balance

$$H\frac{\partial\sigma_s(x,t)}{\partial x} = 2\mu_I[\sigma_c(x,t) + m(x,t)\sigma_s(x,t)]\,. \tag{2}$$

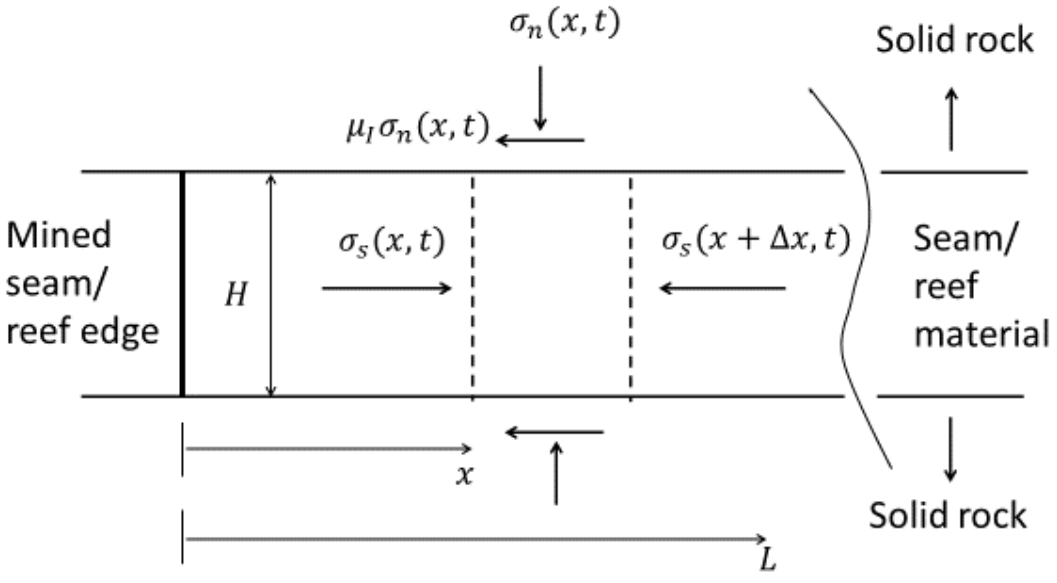

Fig. 2. Force balance for the average reef-parallel confining stress, $\sigma_s(x,t)$, and reef-normal stress, $\sigma_n(x,t)$, at position *x* and time *t* in a plane section erected at right angles to the mining face. The excavation height is *H* and the distance of the fracture zone edge from the mining face is *L*.

The strength envelope, defined by equation (1), that holds at any specific position *x* and time *t* is determined by considering the transition between three bounding, linear strength envelopes having the form of equation (1). The strength of the intact rock is defined by an unconfined strength value σ_c^i and by a slope parameter m_i. Once the material fails, the strength is assumed to drop immediately to an initial limit strength envelope defined by intercept and slope parameters σ_c^0 and m_0 respectively. Once the material has failed, the strength is assumed to decay to a residual strength envelope specified by parameters σ_c^f and m_f. The initial strength drop is suppressed if $\sigma_c^0 = \sigma_c^i$ and $m_0 = m_i$. Similarly, no time-dependent strength decay occurs if $\sigma_c^f = \sigma_c^0$ and $m_f = m_0$.

The transition between the initial limit strength and the residual limit strength envelopes is assumed to be governed by a strength decay function $F(\tau)$ that depends on the elapsed time $\tau = t - T(x)$ between the current time *t* and the initial time of failure, $T(x)$, at point *x*. Specifically, postulate that

$$\sigma_c(x,t) = \sigma_c^f + (\sigma_c^0 - \sigma_c^f)F(t - T(x)) \tag{3}$$

and $$m(x,t) = m_f + (m_0 - m_f)F(t - T(x)), \tag{4}$$

where $F(\tau)$ is the decay function. In the present analysis, it is assumed that, $F(\tau) = 1$ if $\tau < 0$ and that $F(\tau)$ is a simple exponential function of the form

$$F(\tau) = \left(\tfrac{1}{2}\right)^{\tau/\lambda} = e^{-\alpha\tau}, \tag{5}$$

when $\tau \geq 0$. λ is a half-life parameter and the corresponding exponential decay exponent is $\alpha = \ln(2)/\lambda$. The choice of the exponential decay model is supported qualitatively by the application of the time-dependent limit equilibrium model to observed excavation deformations and is able to approximate the characteristic shapes of observed closure profiles (Malan et al[13], Malan and Napier[19]). At the same time it must be emphasized that this particular choice of decay function can be amended, if necessary, within the general numerical treatment discussed later.

Some insight into the time-dependent variation of the confining stress distribution $\sigma_s(x,t)$, can be gained by considering the following boundary value problem. Assume that a parallel-sided panel excavation is suddenly formed at time $t = 0$ and that on each panel edge the abutment fractures

instantly to a distance L_0. (The panel span is not specified explicitly but is understood to be sufficiently large to induce fracturing at each edge.) Only the fracture zone evolution at the right hand edge of the panel is considered. Let $x = 0$ at the right hand edge (see Fig. 2) and postulate that the reef-parallel confining stress is zero at this point:

$$\sigma_s(0,t) = 0\,. \tag{6}$$

In order to facilitate the analysis it is further assumed that the strength parameter functions decay at a proportional rate such that

$$\sigma_c(x,t)/m(x,t) = \sigma_c^0/m_0 = \kappa\,. \tag{7}$$

If equation (7) holds then equation (2) can be expressed as

$$\frac{H}{2\mu_I}\frac{\partial}{\partial x}\{\ln(\sigma_s+\kappa)\} = m(x,t) = m_f + (m_0 - m_f)\exp[-\alpha(t-T(x))]\,, \tag{8}$$

and, subject to the boundary condition (6), can be integrated to yield the solution

$$\frac{H}{2\mu_I}\ln\left[1+\frac{\sigma_s(x,t)}{\kappa}\right] = \int_0^x m(x',t)dx'\,. \tag{9}$$

where $x \le L(t)$ and $L(t)$ is the total fracture zone length at time *t*.

The reef-parallel confining stress $\sigma_s(L,t)$ is assumed to be continuous at the edge of the fracture zone where $x = L(t)$. However, a transition jump may occur between the reef-normal stress component in the limit equilibrium fractured state, designated as $\sigma_n(L^-,t)$, and the reef-normal stress component in the intact state, designated as $\sigma_n(L^+,t)$. From the definition of the initial limit strength envelope parameters and the intact rock strength parameters, it can be inferred that

$$\sigma_n(L^-,t) = \sigma_c^0 + m_0\sigma_s(L(t),t)\,, \tag{10}$$

and $$\sigma_n(L^+,t) = \sigma_c^i + m_i\sigma_s(L(t),t)\,. \tag{11}$$

Let $\sigma_n^* = \sigma(L^+,t)$ and hence, from equation (11),

$$\sigma_s(L(t),t) = \sigma_s^* = (\sigma_n^* - \sigma_c^i)/m_i\,. \tag{12}$$

In order to find an analytic expression for $L(t)$, the critical assumption is made that σ_n^* remains approximately constant as the fracture front extends. This is intuitively plausible if the panel span is

relatively large compared to the length of the fracture zone. Substituting $x = L(0) = L_0$ into equation (9) and noting that at time zero $m(x,0) = m_0$, the value of the initial crush zone length L_0 is

$$L_0 = \frac{H}{2\mu_I m_0} \ln\left[1 + \frac{\sigma_s^*}{\kappa}\right]. \tag{13}$$

In the region $0 \le x \le L_0$ the function $m(x,t)$ is a function of *t* only since $T(x) = 0$. Using equations (4) and (5) this becomes

$$m(x,t) = m_f + (m_0 - m_f)e^{-\alpha t}, \ 0 \le x \le L_0. \tag{14}$$

Setting $x = L(t)$ in equation (9) and employing equations (12) and (14), yields

$$\frac{H}{2\mu_I} \ln\left[1 + \frac{\sigma_s^*}{\kappa}\right] = \left[m_f + (m_0 - m_f)e^{-\alpha t}\right] L_0 + \int_{L_0}^{L(t)} m(x,t)dx. \tag{15}$$

Differentiating equation (15) with respect to *t* and using Leibniz formula gives

$$-\alpha L_0 (m_0 - m_f)e^{-\alpha t} + m_0 \frac{dL}{dt} + \int_{L_0}^{L} \frac{\partial m(x,t)}{\partial t} dx = 0, \tag{16}$$

where it is noted that $m(L,t) = m_0$. From equation (4) and the assumed exponential decay function (5), it can be shown that

$$\frac{\partial m(x,t)}{\partial t} = \alpha\left[m_f - m(x,t)\right], \tag{17}$$

and therefore, using equations (15) and (13), equation (16) can be expressed in the form

$$\frac{dL}{dt} + (\alpha m_f / m_0)L = \alpha L_0. \tag{18}$$

Equation (18) is a simple first order linear differential equation which can be solved with the boundary condition $L(0) = L_0$. The solution is

$$L(t) = L_f + (L_0 - L_f)\exp(-\alpha m_f t / m_0), \tag{19}$$

where $\lim_{t\to\infty} L(t) = L_f$ and

$$L_f = m_0 L_0 / m_f = \frac{H}{2\mu_I m_f} \ln\left[1 + \frac{\sigma_s^*}{\kappa}\right]. \tag{20}$$

Using the half-life relationship $\alpha = \ln(2)/\lambda$, equation (19) can be expressed in the non-dimensional form:

$$L(t)/L_f = 1-(1-M_f)\left(\frac{1}{2}\right)^{M_f t/\lambda}, \tag{21}$$

where $M_f = m_f / m_0 = L_0 / L_f$. (22)

Fig. 3 is a plot of equation (21) for three selected values of the scaled slope parameter ratio M_f and shows the exponential time-dependent evolution of the fracture zone length.

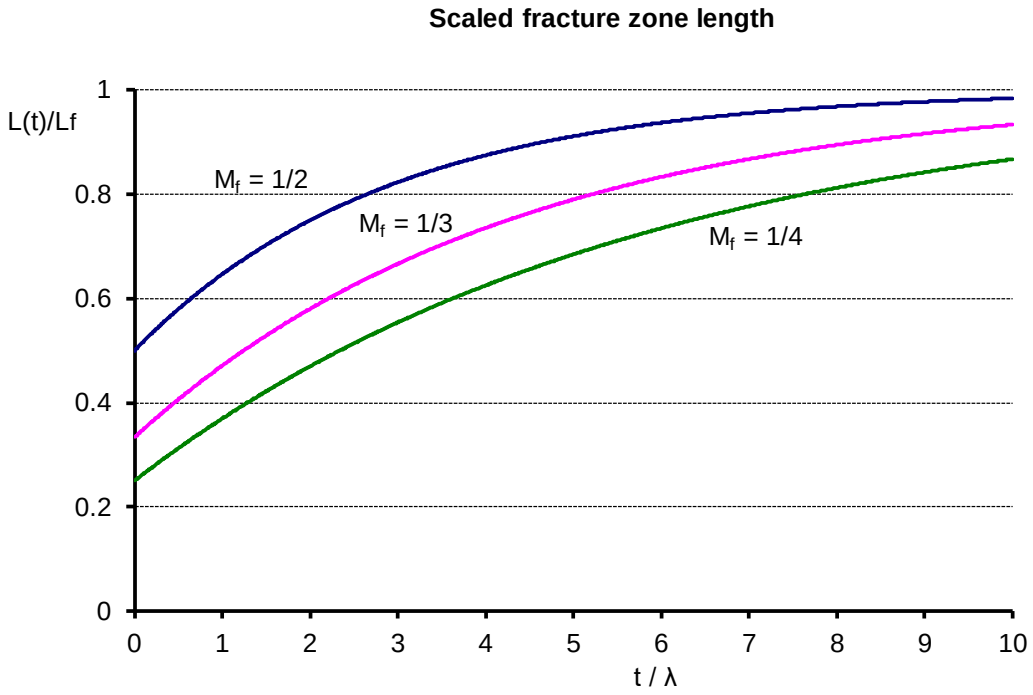

Fig. 3. Scaled fracture zone length as a function of the elapsed time scaled to the half-life decay time λ.

Conversely, equation (21) can be inverted to define the time $t = T(x)$ at which failure is initiated at the coordinate position $x = L(t)$. Solving equation (21) for *t* yields the scaled failure initiation time

$$T(x)/\lambda = \frac{1}{M_f}\log_2\left[\frac{1-M_f}{1-(x/L_f)}\right]. \tag{23}$$

It is useful to define a scaled slope ratio function $M(x,t)$ as follows:

$$M(x,t) = m(x,t)/m_0 . \tag{24}$$

Employing the exponential decay function, given by equation (5), and substituting the value of $T(x)$ given by equation (23) into equation (4) yields the slope ratio function in the explicit form

$$M(x,t) = M_f + (1-M_f)\left(\frac{1}{2}\right)^{t/\lambda}\left[\frac{1-M_f}{1-(x/L_f)}\right]^{1/M_f}, \tag{25}$$

where $L_0 \le x \le L(t)$. Since $L_0/L_f = M_f$, it can be seen that

$$M(L_0,t) = M_f + (1-M_f)2^{-t/\lambda}, \tag{26}$$

and, from equation (21), $M(L(t),t) = 1$. The slope ratio function is plotted in Fig. 4 using the specific parameter value $M_f = 1/3$ with four values of the elapsed time t/λ indicating the progressive evolution of the slope ratio function $M(x,t)$ as the fracture zone evolves.

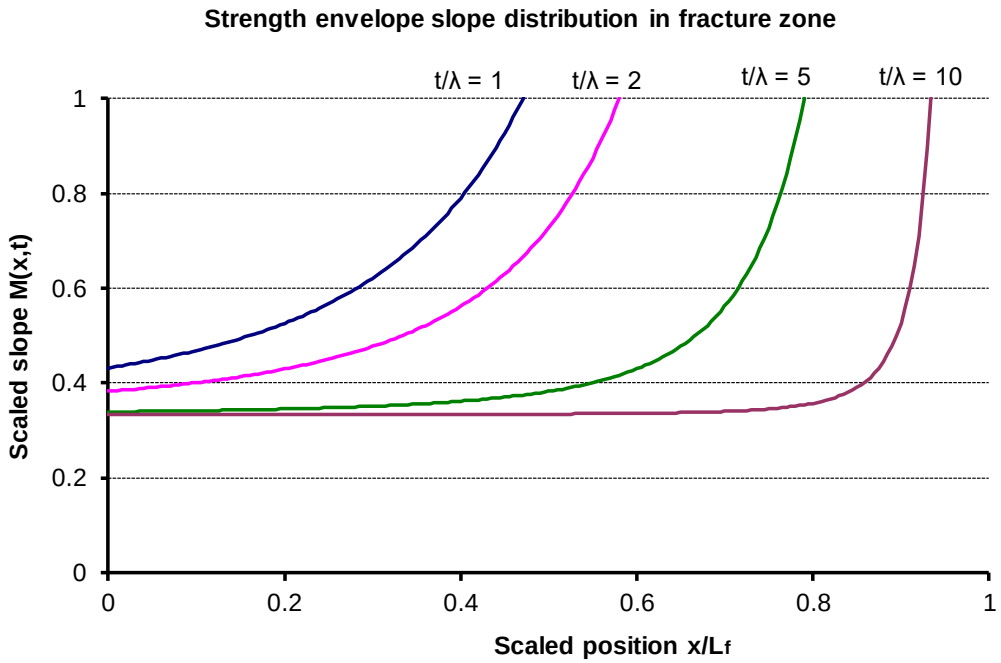

Fig. 4. Distribution of the scaled limit strength slope function $M(x,t)$ profile within the fracture zone at different times for the slope ratio parameter $M_f = 1/3$.

3. Tabular excavation numerical solution

The solution of tabular layout problems using the displacement discontinuity method has been extensively reported (for example, Crouch and Starfield[9], Salamon[10,20], Deist et al[21], Ryder and Napier[22], Napier and Malan[23], Peirce et al[24], Spottiswoode and Drummond[25]). In a general tabular layout analysis, the regions of interest (for example, the layout shown in Fig. 1) are assumed to be planar and are tessellated using square or triangular displacement discontinuity elements. It is assumed in this paper that the excavation plane is horizontal and only stress and displacement components normal to the excavation surface are considered. Let $D_n(Q,t)$ be the normal displacement discontinuity component at point *Q* and time *t*, defined to be the difference between the normal displacement vector components on opposite sides of the excavation plane. Specifically, define

$$D_n(Q,t) = u_n^-(Q,t) - u_n^+(Q,t), \tag{27}$$

where $u_n^+(Q,t)$ is the displacement vector component on the excavation surface side corresponding to the positive direction of an assigned normal vector and $u_n^-(Q,t)$ is the displacement vector component on the opposite side at time *t*. The convention used in equation (27) ensures that $D_n(Q,t) > 0$ if the roof and floor of the excavation move towards one another and will be referred to as the excavation closure or elastic convergence. The time dependence is included explicitly since the fracture zone deforms and extends continually.

It is postulated as well that the displacement discontinuity elements are square with a grid size *g*. A single collocation point is located at the element centre representing the average displacement discontinuity value in the element. The normal traction component $\sigma_n(P,t)$ at a collocation point *P* and time *t* is determined by the relationship

$$\sigma_n(P,t) = \sigma_n^V(P) + \sum_Q K(P,Q) D_n(Q,t), \tag{28}$$

where $\sigma_n^V(P)$ is the primitive field stress component at point *P*. The term $K(P,Q)$ in equation (28) represents a stress influence matrix that depends only on the relative coordinate positions x_P, y_P and x_Q, y_Q of points *P* and *Q* in the excavation plane. Specifically, if $x_P - x_Q = ig$ and $y_P - y_Q = jg$ where *i* and *j* are integers then

$$K(P,Q) = \frac{E}{8\pi(1-\nu^2)g} M_{ij}. \tag{29}$$

E and ν are the host rock Young's modulus and Poisson's ratio respectively and M_{ij} is given by

$$M_{ij} = \frac{[(i-\frac{1}{2})^2 + (j-\frac{1}{2})^2]^{1/2}}{(i-\frac{1}{2})(j-\frac{1}{2})} - \frac{[(i-\frac{1}{2})^2 + (j+\frac{1}{2})^2]^{1/2}}{(i-\frac{1}{2})(j+\frac{1}{2})}$$

$$- \frac{[(i+\frac{1}{2})^2 + (j-\frac{1}{2})^2]^{1/2}}{(i+\frac{1}{2})(j-\frac{1}{2})} + \frac{[(i+\frac{1}{2})^2 + (j+\frac{1}{2})^2]^{1/2}}{(i+\frac{1}{2})(j+\frac{1}{2})} . \qquad (30)$$

When $i = j = 0$, $K(P,Q) = K_{00} = \sqrt{2}E/[\pi(1-\nu^2)g]$ represents the local self-effect kernel stiffness. Equation (28) can be solved iteratively for the unknown discontinuity components $D_n(Q,t)$ provided the traction values $\sigma_n(P,t)$ are specified at each collocation point. These values are set to zero at open excavation points but require special treatment at points in the time-dependent fracture zone region adjacent to the excavation edges where $\sigma_n(P,t)$ depends on the reef-parallel stress distribution $\sigma_s(P,t)$. For a planar excavation embedded in three-dimensional space, the confining stress gradient $\nabla\sigma_s(P,t)$ in the fracture zone is a function of two local spatial coordinates in the layout plane and equation (2) is replaced by the expression:

$$H\left|\nabla\sigma_s(P,t)\right| = 2\mu_1 m(P,t)[\kappa + \sigma_s(P,t)], \qquad (31)$$

where it is again noted that

$$\sigma_c(P,t)/m(P,t) = \sigma_c^0/m_0 = \kappa .$$

A fast marching scheme has been developed to solve the eikonal equation (31) in a series of time steps to solve the evolving strength parameters and the reef-parallel confining stress distribution following the initiation of fracture at each point *P* (see Napier[26]). The reef-normal component $\sigma_n(P,t)$ is inferred from the assumed strength relationship

$$\sigma_n(P,t) = \sigma_c(P,t) + m(P,t)\sigma_s(P,t), \qquad (32)$$

and is used as the boundary condition traction in equation (28).

The solution is obtained in a series of time step cycles using the following general procedure:

(i) Adjust the layout geometrical configuration corresponding to the specified mining schedule at the current time.

(ii) Adjust the values of the time-dependent strength parameters at all failed fracture zone points for the current time step. Use the fast marching scheme[26] to solve the fracture zone confining stress distribution in the current layout configuration.

(iii) Solve the layout element assembly for the displacement discontinuity values. Update the current fracture zone extent.

(iv) Exit if the specified mining schedule is completed or advance the time step increment and return to step (i).

4. Grid size effects

The simplest computational scheme that can be devised to solve the time-dependent fracture zone model is to assume that the element collocation points in the unmined region are either intact or are in the failed limit strength state. In the intact state, at a given point *P*, the displacement discontinuity component is set to zero but is adjusted appropriately to reflect the limit strength value $\sigma_n(P,t)$ in the failed state. Using this approach it is apparent that the exact fracture zone edge position cannot be located to a resolution that is finer than the chosen element grid size, *g*. When using the time-dependent strength decay model the fracture zone may therefore extend abruptly when the stress levels in intact elements reach the defined intact rock strength limit. The magnitude of the change in the distribution of the displacement discontinuity solution values corresponding to this change is dictated by the element grid size. When the fracture zone extent ahead of the mining face is of the order of the element size this can lead to sudden changes in simulated time-dependent closure profiles at open excavation points. As the element size is reduced, these sudden changes are progressively reduced. Run time penalties associated with small grid sizes can become significant in the case of large-scale layout analyses.

Several computational strategies can be used to improve the solution efficiency for large element assemblies. These include the use of hierarchical numerical schemes (so-called "lumping" methods, for example, Napier and Malan[23]) or efficient influence computation using fast-Fourier methods to solve the layout configuration (Peirce et al[24], Spottiswoode and Drummond[25]). A useful strategy for intermediate sized problems, comprising a single mining horizon tessellated with square elements, is to pre-calculate and store the influence matrix defined by equation (30). This special-purpose solution approach is employed in the current work but limits problem sizes to approximately 100000 elements on laptop or desktop computers.

An additional strategy has been developed to smooth sudden changes in the fracture zone edge location by introducing a novel partial element failure construction. This is illustrated most easily for the case where the confining stress gradient depends on a single coordinate position *x* as shown in Fig. 5. The fracture front is estimated at a general position $x = L$ within the boundaries of a specific element. The procedure employs the known solution state $\sigma_s(x_e,t) = \sigma_s^e$ at the closest fully failed neighbour element collocation point, $x = x_e$ to infer the offset distance $R = L - x_e$ between this

"anchor" point and the fracture zone edge. Integrating equation (8) between the limits $x = x_e$ and $x = L$ yields

$$\frac{H}{2\mu_I} \ln\left[\frac{\sigma_s(L,t)+\kappa}{\sigma_s(x_e,t)+\kappa}\right] = \int_{x_e}^{L} m(x,t)dx \cdot \tag{33}$$

If a plausible estimate can be made for the value of $\sigma_s(L,t) = \sigma_s^*$ and if the functional form for $m(x,t)$ can be suitably approximated then equation (33) can be solved to provide an estimate for the fracture edge position $x = L$.

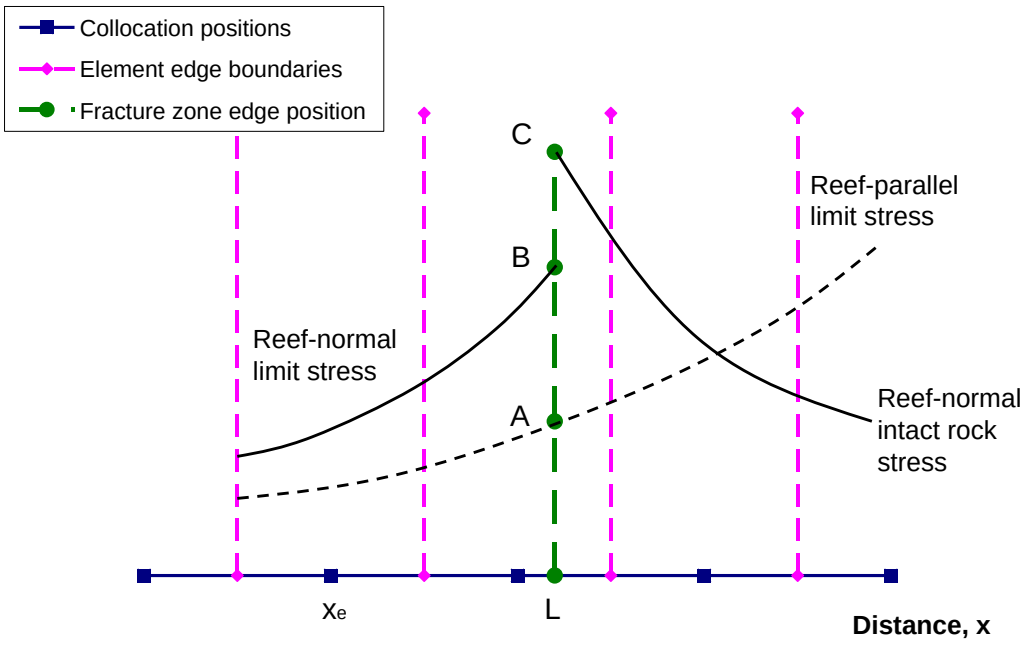

Fig. 5. Schematic stress profiles adjacent to the edge of the fracture zone imposed on a local element mesh. The element collocation point positions are designated by square markers and the element junction positions are highlighted.

Let the intact rock stress at point C in Fig. 5 be $\sigma_n^r = \sigma_n(L^+,t)$ then, from equation (12),

$$\sigma_s^* = \sigma_s(L,t) = (\sigma_n^r - \sigma_c^i)/\bar{m}_i, \tag{34}$$

where $\bar{m}_i$ is an estimate of the effective intact strength slope parameter in the edge element region that is assumed to be given by

$$\bar{m}_i = (m_0 + m_i)/2 . \tag{35}$$

Employing the strength ratio definition, $\kappa = \sigma_c^0 / m_0$ it appears that

$$\left[\frac{\sigma_s(L,t)+\kappa}{\sigma_s(x_e,t)+\kappa}\right] \approx \frac{\sigma_c^0 + (m_0/\bar{m}_i)(\sigma_n^r - \sigma_c^i)}{\sigma_c^0 + m_0\sigma_s^e} . \tag{35}$$

The choice of the function shape for $m(x,t)$ in the interval $x_e \le x \le L$ is constrained by the condition that the limit slope $m(x_e,t) = m_e$ is known at $x = x_e$ and by $m(L,t) = m_0$ at the fracture zone edge. In addition, it is apparent from Fig. 4 that the slope of the function $m(x,t)$ can become very large when $x \sim L$. Assuming that in the extreme case this slope is infinite, an approximate form for $m(x,t)$ is the function

$$m(x,t) \sim m_0 - [m_0 - m(x_e,t)]\sqrt{\frac{L-x}{L-x_e}} \quad \text{for } x_e \le x \le L . \tag{36}$$

Substituting equations (35) and (36) into equation (33) and performing the integration yields the expression for the offset distance *R* as

$$R = L - x_e = \frac{3H}{2\mu_I(m_0 + 2m_e)} \ln\left[\frac{\sigma_c^0 + (m_0/\bar{m}_i)(\sigma_n^r - \sigma_c^i)}{\sigma_c^0 + m_e\sigma_s^e}\right]. \tag{37}$$

The evaluation of the fracture front offset distance *R* can be incorporated in the iterative solution of equation (28) at all intact fracture zone collocation points that are adjacent to any completely failed neighbour element. As a simplification, the failed element neighbour confining stress gradient direction is identified to fall in one of eight sectors as illustrated in Fig. 6. The appropriate sector for the failed neighbour anchor point is chosen according to the local reef-parallel stress gradient direction at the centre point P_0 in Fig. 6. The edge offset distance *R* is evaluated using equation (37) using the current values of σ_s^e and m_e at the centre of the failed neighbour element. The rock stress σ_n^r is approximated by the total external induced stress at point P_0 in Fig. 6. Explicitly, from equation (28),

$$\sigma_n^r \approx \sigma_n^V(P_0) + L_n(P_0,t) + E_n(P_0,t) . \tag{38}$$

The terms $L_n(P_0,t)$ and $E_n(P_0,t)$ in equation (38) represent partial sums of the right hand side of equation (28) that are taken, respectively, over the eight immediate neighbour elements to P_0 in Fig. 6

and over all remaining elements external to both P_0 and the local immediate neighbour elements. This partitioning is used in the sub-element logic described below.

It is evident from Fig. 6 that the failed neighbour may be either in a sector directly adjacent to the central element side of length g or along one of the central element diagonal directions. The fraction ϕ of the central element that is deemed to be fractured is therefore given by

$$\phi = \frac{R}{g} - \frac{1}{2};\ g/2 \le R \le 3g/2, \tag{39}$$

for a side element neighbour. The fracture fraction for a diagonal neighbour is given by

$$\phi = \left[\frac{R}{g} - \frac{1}{\sqrt{2}}\right]^2 \text{ if } g/\sqrt{2} \le R \le \sqrt{2}g \tag{40}$$

and $$\phi = 1 - \left[\frac{3}{\sqrt{2}} - \frac{R}{g}\right]^2 \text{ if } \sqrt{2}g < R \le 3g/\sqrt{2}. \tag{41}$$

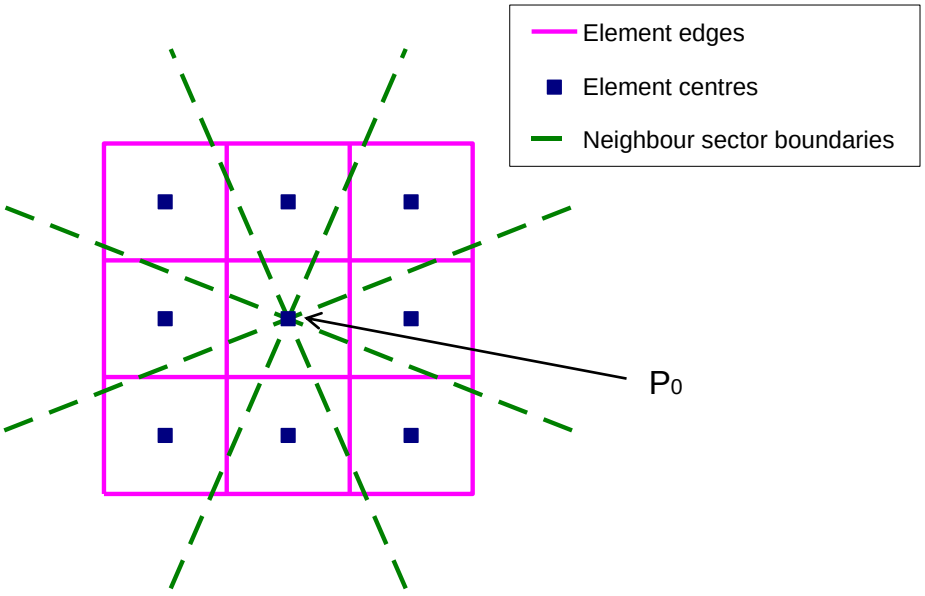

Fig. 6. Neighbour gradient sector partitions for a square element with centre P_0. Each element side has length g.

Once the failed fraction ϕ has been determined, a fractional sub-element with an appropriate shape, centre position and self-effect coefficient $\hat{K}_{00}$ is constructed within the central element region of Fig.

6. The total stress $\hat{\sigma}_n$ at the sub-element centre is assumed to be given by the limit equilibrium strength relationship

$$\hat{\sigma}_n = \sigma_c^0 + m_0 \hat{\sigma}_s, \tag{42}$$

where the local reef-parallel confining stress $\hat{\sigma}_s$ is determined by interpolating the fast marching grid solution values at the sub-element centre. The sub-element closure $\hat{D}_n$ is determined during the iterative cycle processing of point P_0 by solving a local adapted version of equation (28) which can be expressed as

$$\hat{\sigma}_n = \hat{K}_{00} \hat{D}_n + \sigma_n^V(P_0) + \hat{L}_n + E_n(P_0, t), \tag{43}$$

where $\hat{L}_n$ is a modified influence sum evaluated at the sub-element centre which replaces the sum $L_n(P_0, t)$ for the eight local neighbours surrounding P_0. In order to maintain the uniform grid structure for far-field influence transmission purposes, the local sub-element displacement discontinuity value $\hat{D}_n$ is replaced by the average element value $D_n(P_0, t) = \phi \hat{D}_n$.

In order to illustrate the performance of the partial element fracturing algorithm, consider the case of a simple rectangular excavation having an initial span of 30.0 m and a panel length of 31.0 m. An initially intact 20.0 m by 31.0 m rectangular abutment region is assumed to exist adjacent to one panel edge. The nominal element grid size, *g*, is chosen to be one metre and the overall model region falls within a 50.0 m by 31.0 m rectangle. The chosen rock material constants and limit equilibrium failure parameters are summarised in Table 1. For the purposes of the grid size test, it is assumed that the initial 30 m by 31 m excavation is created instantly and that the solid abutment region adjacent to the panel edge is allowed to fail for a time period of 100 time units. Following this initial relaxation phase the panel edge is advanced in five increments of one metre within the abutment region, at intervals of 10 time units. The final elapsed time is 150 units and the final mined span is 35.0 m. The total area A_F of the crushed fracture zone elements is noted at each time step and the average fracture zone length in the direction of mining is defined to be $L_{avg} = A_F / 31\,\text{m}$, using the assumed panel length of 31 m.

Three cases are considered. In the first case, it is assumed that fracturing occurs discretely in each crush zone element having a grid size of 1.0 m. The analysis is then repeated with the grid size reduced to 0.2 m (the total number of elements is increased by a factor of 25). Each crush zone element is deemed to be either intact or fully failed as for the coarse element case. A final analysis is performed with the grid size set to 1.0 m but allowing partial fracturing of the crush zone elements at

the edge of the fracture zone. The average length of the fracture zone as a function of the simulated time step number is shown for each case in Fig. 7. The analytic result for the fracture zone length, given by equation (19), is included in Fig. 7 for the initial relaxation time period of 100 units. It is assumed in the analytic expression (19) that the initial fracture zone length is $L_0 \approx 1.94$ m and that $L_f / L_0 = m_0 / m_f = 4$.

It is apparent immediately from Fig. 7 that the coarse grid results with discrete element fracturing is consistently lower than the fracture zone length profile obtained for the fine grid simulation. The partial fracturing algorithm does however match the fine grid results much more satisfactorily in both the initial relaxation phase (time steps 1 to 100) and in the subsequent mining phase where the fracture zone length is abruptly altered following each mining step increment. In addition, both the fine grid and the partial element average fracture length profiles can be seen to correspond approximately to the analytic fracture zone length profile in the initial relaxation time period. These results indicate that the partial element fracturing algorithm can be used to avoid mesh-dependent effects in large scale simulations while retaining the computational efficiency of a larger grid size.

Table 1. Parameters used to illustrate the performance of the partial element fracture algorithm.

Intact strength intercept, $\sigma_c^{\,i}$	60.0 MPa
Intact strength slope, m_i	6.0
Initial residual strength intercept, $\sigma_c^{\,0}$	40.0 MPa
Initial residual strength slope, m_0	4.0
Final residual strength intercept, $\sigma_c^{\,f}$	10.0 MPa
Final residual strength slope, m_f	1.0
Effective seam height, H	3.0 m
Intact rock Young's modulus, E	72000.0 MPa
Intact rock Poisson's ratio, v	0.2
Intact seam stiffness modulus, k_s	Rigid
Fracture zone interface friction angle, φ_I	20 degrees
Fracture zone strength half-life parameter, λ	40.0 time units
Vertical field stress at panel horizon	100.0 MPa

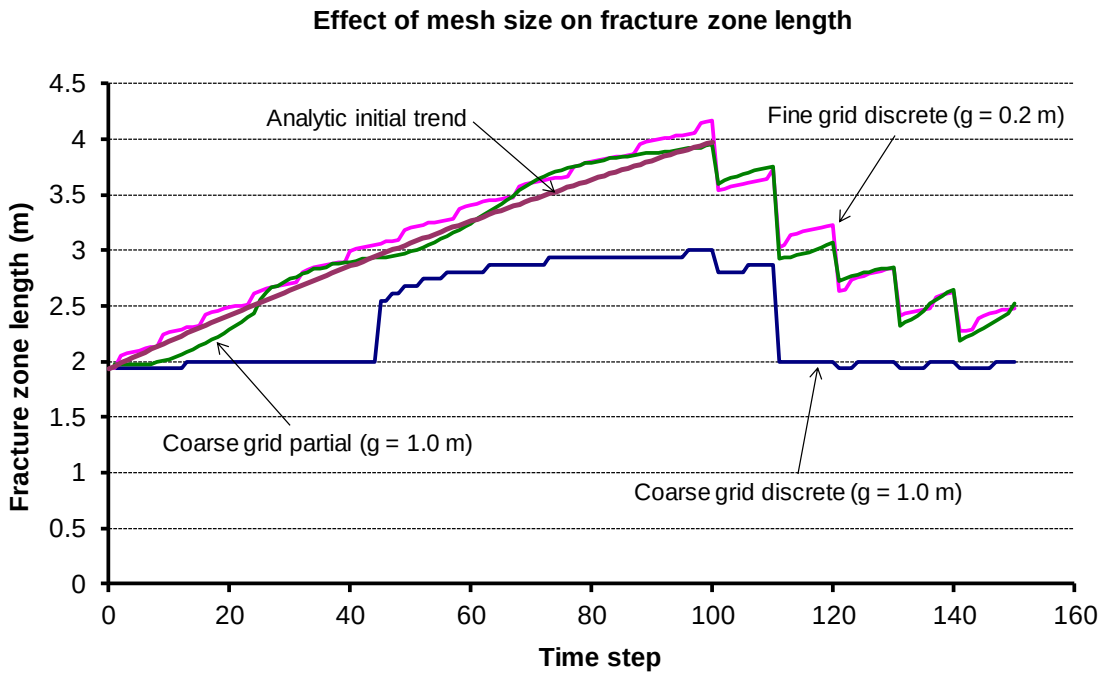

Fig. 7. Illustration of the effect of different grid size choices on the estimated fracture zone length developed in the simple mining panel shown in Fig. 11.

5. Rate of mining and face advance increment selection

In order to illustrate the effect of changing the mining rate and the face advance increment step size, consider the simple case of the two adjacent 25 m panels A and B shown in Fig. 8. The rock strength properties are considered to be uniform in the fracture zone region and are the same as those reported in Table 1. The field stress at the excavation horizon is chosen to be 80 MPa in this case. The initial excavation closure in the mined region shown in Fig. 8 is first solved and the fracture zone is allowed to relax for 20 time steps. It is emphasized again that previous studies (Malan and Napier[19]) have indicated that the time-dependent limit equilibrium model can replicate recorded time-dependent closure profiles for tabular stope geometries. This is encouraging as simple viscoelastic models cannot simulate all the spatial aspects of time-dependent convergence recorded in tabular excavations.

Three alternative mining schedules are considered following this initial relaxation phase:

1. Panel A and Panel B are advanced by 1.0 m on alternate "days" where each day is assumed to have a duration of 10 time step intervals. The area mined as a function of time corresponds to a so-called "Slow" mining schedule. (The total area mined is equal to 1500 m^2 and the total number of time steps is equal to 600. Element size, g = 1.0 m)

2. Panel A and Panel B are both advanced by 1.0 m every day. The mining rate is effectively doubled and corresponds to a "Fast" mining schedule. (The total area mined is equal to 1500 m^2 and the total number of time steps is equal to 300. Element size, g = 1.0 m)
3. Panel A and Panel B are both advanced by 0.5 m every day. The mining rate is now equivalent to the "Slow" rate that occurs in schedule 1. (The total area mined is equal to 1500 m^2 and the total number of time steps is equal to 600. Element size, g = 0.5 m)

No consideration is given here to the important practical question of the relative cost of each of these mining options. Schedule 3 may be the most expensive option in terms of mining crew availability but may be considered as a necessary strategic choice to reduce face instability.

Fig. 9 shows the final fracture zone extent at the completion of mining schedule 1. The partially fractured elements are distinguished at the edge of the fracture zone. The corresponding fracture zone region at the end of mining schedule 2 is shown in Fig. 10. It can be seen in this case that the final fracture zone extent is somewhat smaller than for the "slow" mining fracture zone in Fig. 9. A clearer distinction between the mining rate schedules can be obtained by considering the overall incremental energy release in each mining step.

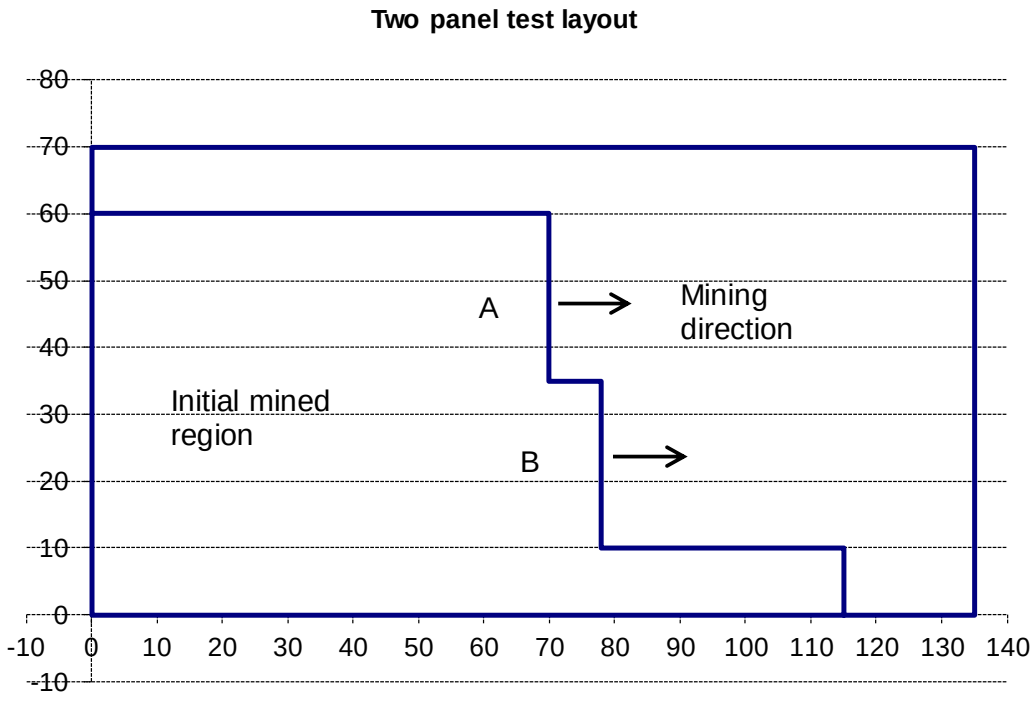

Fig. 8. Test layout to evaluate mining rate and face advance variations in two adjacent panels.

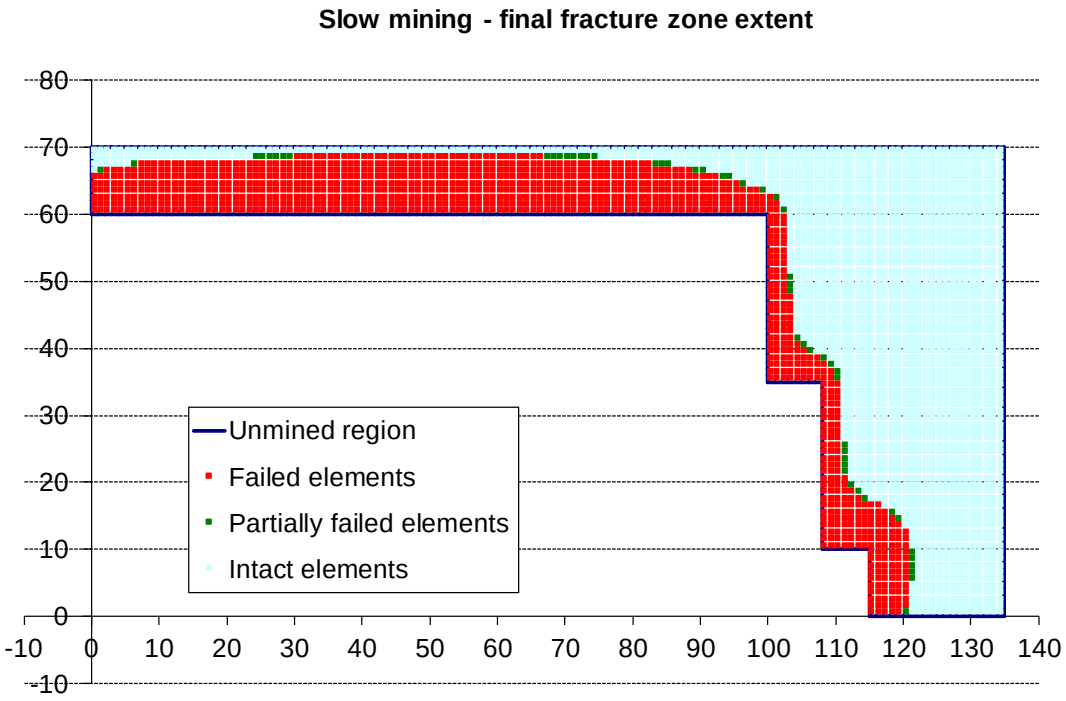

Fig. 9. Final fracture zone extent for slow mining schedule with uniform strength properties and grid size g = 1.0 m.

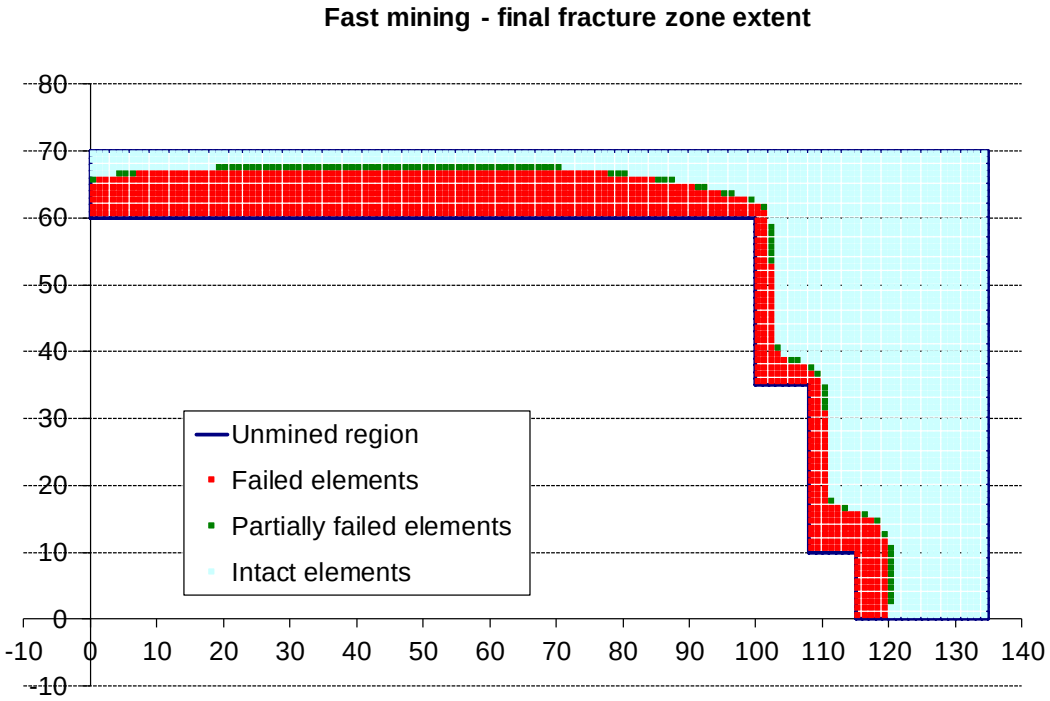

Fig. 10. Final fracture zone extent for fast mining schedule with uniform strength properties and grid size g = 1.0 m.

The energy release face stability measure is determined by calculating the overall energy balance between each time step solution state and summing the energy release changes that are not accounted for by rock crushing dissipation processes or by strain energy changes. Details of these energy release calculations are given by Napier and Malan[14] and are not repeated here. The main purpose of this face stability measure is to provide a surrogate indication of the likely level of seismic activity following each mining step and an indication of the possible occurrence of further unstable deformations between the face advance steps.

The simulated energy release increments corresponding to each mining schedule are presented in Fig. 11. This shows that the major increments in released energy arise when each mining step occurs and that significantly greater increments occur when the "fast" mining schedule is executed. It is apparent as well from Fig. 11 that the energy release increments are relatively uniform in each extraction schedule and that very little additional background energy is released between each mining step.

The most interesting and significant observation in Fig. 11 is that the energy release increments associated with mining schedule 3, in which the face advance increment is reduced to 0.5 m, are significantly smaller than in schedule 1 where the face advance increment is 1.0 m. In order to affirm this observation, the three mining schedules were repeated with the uniform rock strength properties replaced by the random strength properties given in Table 2 and with the alternative simulation parameters summarised in Table 3. These parameters were arbitrarily selected to demonstrate the behaviour of the model. Additional work is required in future to calibrate these parameters. For example, time-dependent stope closure data can be used to calibrate the half-life parameter, λ (Malan and Napier[19]).

The revised energy release increments for each mining schedule are depicted in Fig. 12. It is clear that the random strength properties lead to a significantly greater variability in the distribution of the energy release increment magnitudes. However, the energy release increments associated with schedule 3, in which the face advance is reduced to 0.5 m, are still significantly lower (on average) than for the results of schedule 1 where the face advance increment is 1.0 m. This trend is confirmed in Fig. 13 where the cumulative energy release values are plotted for each mining schedule. This finding is in qualitative agreement with what has been known for many years in the deep gold mines of South Africa. In areas subjected to high stress and those prone to seismicity, it appears to be beneficial to use short hole lengths (0.5 m) for the production holes compared to the typical normal hole length of 0.9 m. The Chamber of Mines Research Organisation recommended that for remnants the face advance per blast should not exceed 0.6 times the stoping width[27]. Jager and Ryder[28] recommended for remnant mining that the advance per blast should be kept as small as possible.

Fig. 14 and Fig. 15 show the individual comparisons between the energy release increments for random and uniform rock strength properties for mining schedules 1 and 3 respectively. This emphasises the variability induced by the random strength properties as well as the higher levels of activity that arise between each face advance increment when the random strength properties are considered. However, the comparison between Fig. 14 and Fig. 15 reinforces the conclusion that the short face advance distance adopted in schedule 3 can be beneficial in reducing the overall energy release levels.

The small variability of the uniform strength energy release increments observed is related to both the longer half-life decay parameter of 40 time units (see Table 1 and Table 3) and to the assignment of the uniform rock strength values. It should be emphasised though that there is no inherent connection between the uniform and random strength average levels of energy release in terms of the arbitrarily assigned material properties and the vertical field stress that is assumed in each case. The average energy release level in each case can be adjusted by amending the strength and half-life parameters. The appropriate assignment of these parameter values requires additional field data calibration. However, the main conclusion is that the model can be used to distinguish practical choices in the extraction rate schedule and the face advance increment size.

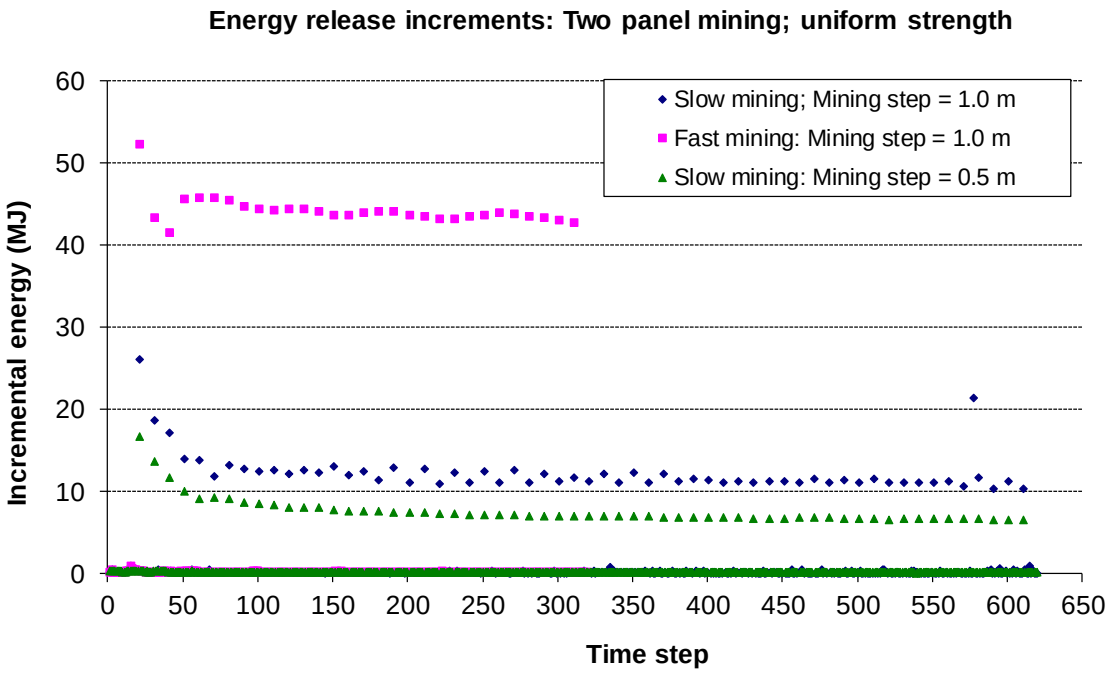

Fig. 11. Energy release increments observed in each time step corresponding to the three mining schedules applied to the test panel layout shown in Fig. 8 with uniform strength properties given in Table 3.

Table 2. Intact and initial failure strength parameters assigned at random to each fracture zone element.

	Intact strength intercept (MPa)	Intact strength slope	Initial failure strength intercept (MPa)	Initial failure strength slope
1	10.0	1.0	10.0	1.0
2	17.0	1.7	14.0	1.4
3	24.0	2.4	18.0	1.8
4	31.0	3.1	22.0	2.2
5	38.0	3.8	26.0	2.6
6	45.0	4.5	30.0	3.0
7	52.0	5.2	34.0	3.4
8	59.0	5.9	38.0	3.8
9	66.0	6.6	42.0	4.2
10	73.0	7.3	46.0	4.6

Table 3. Limit equilibrium model parameters used in the random strength test runs.

Final residual strength intercept, σ_c^f	10.0 MPa
Final residual strength slope, m_f	1.0
Effective seam height, H	3.0 m
Intact rock Young's modulus, E	72000.0 MPa
Intact rock Poisson's ratio, v	0.2
Intact seam stiffness modulus, k_s	Rigid
Fracture zone interface friction angle, φ_I	20 degrees
Fracture zone strength half-life parameter, λ	20.0 time units
Vertical field stress at panel horizon	100 MPa

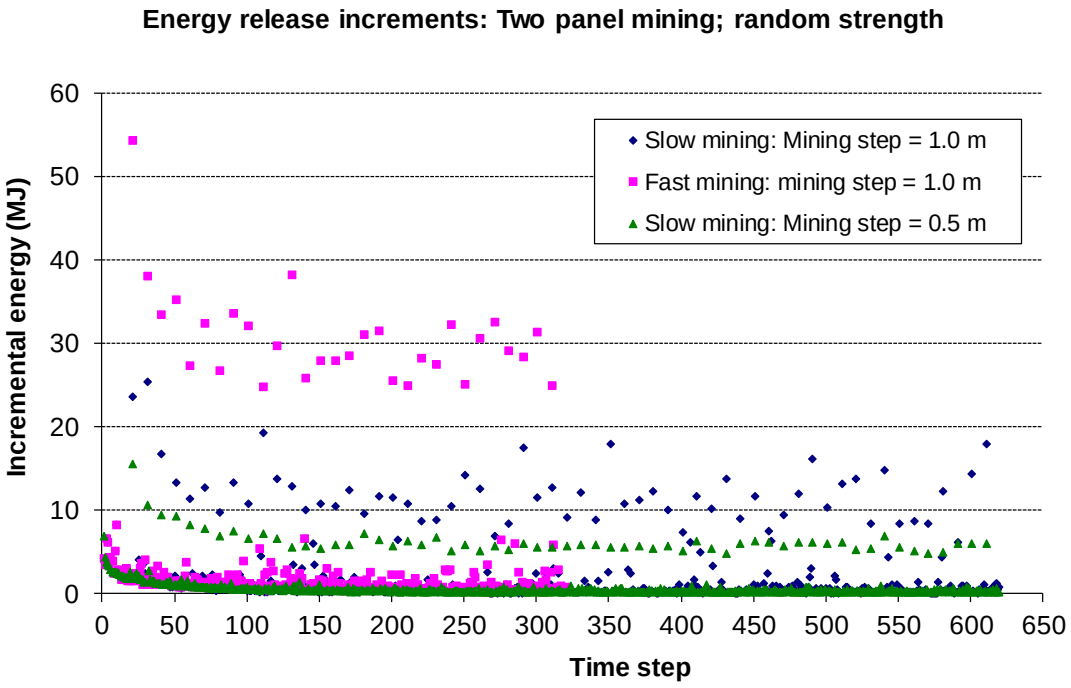

Fig. 12. Energy release increments observed in each time step corresponding to the three mining schedules applied to the test panel layout shown in Fig. 8 (random strength properties given in Tables 1 and 2).

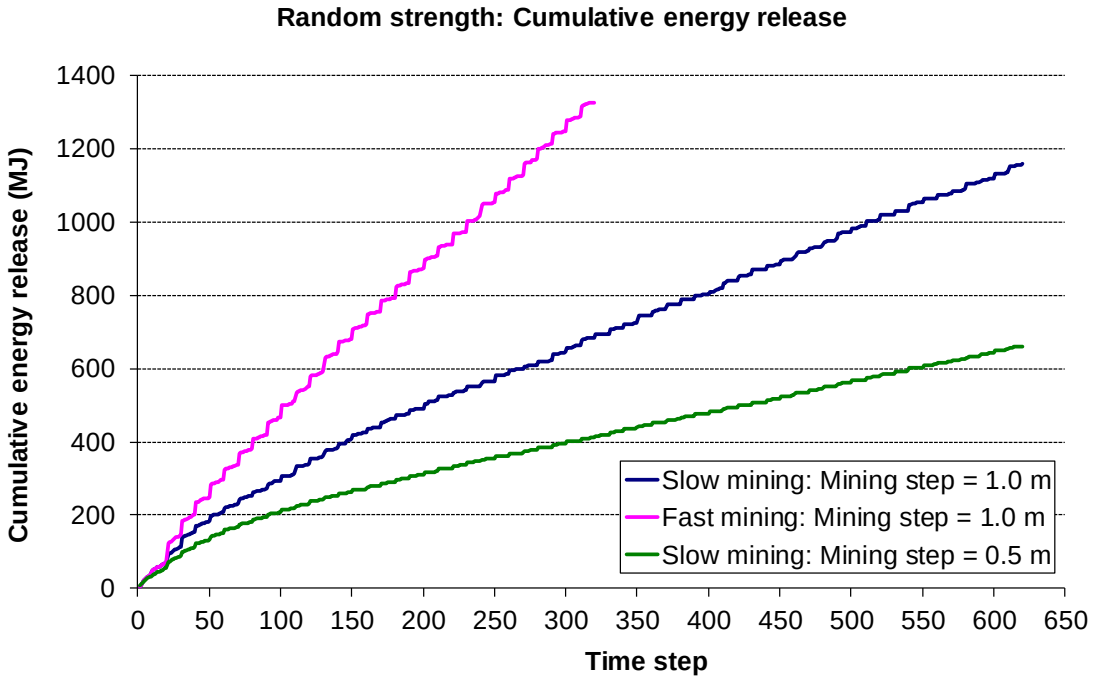

Fig. 13. Cumulative energy release increments observed in each time step corresponding to the three mining schedules applied to the test panel layout shown in Fig. 8 (random strength properties given in Tables 1 and 2).

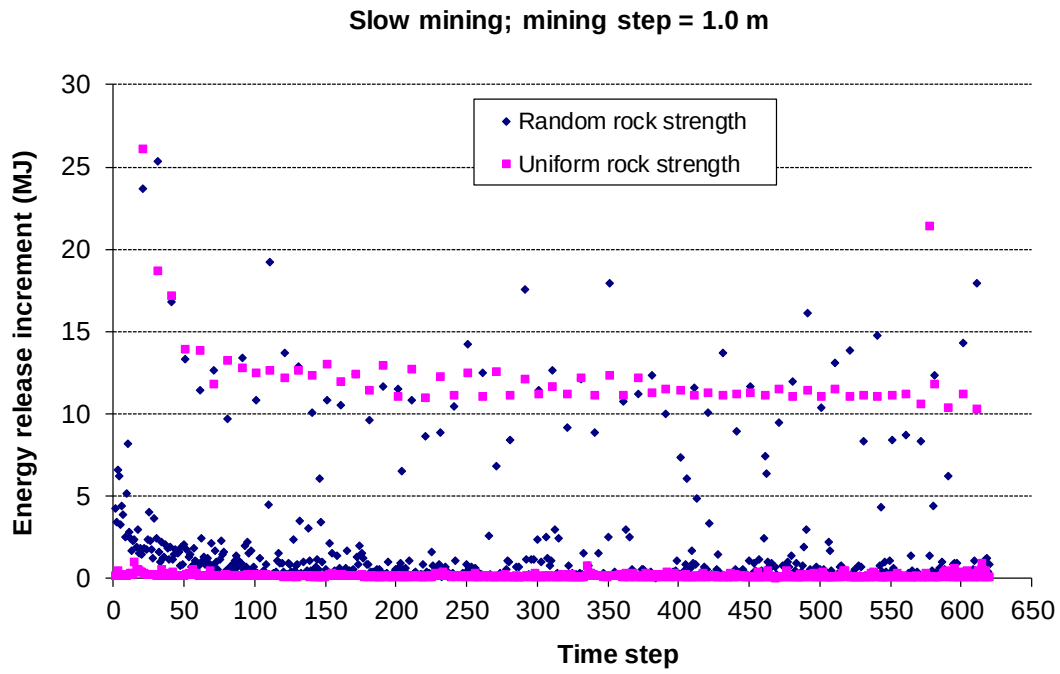

Fig. 14. Comparison between the energy release increments in each mining step when random rock strength and uniform rock strength properties are used. (Slow mining rate with face advance increment = 1.0 m; schedule 1.)

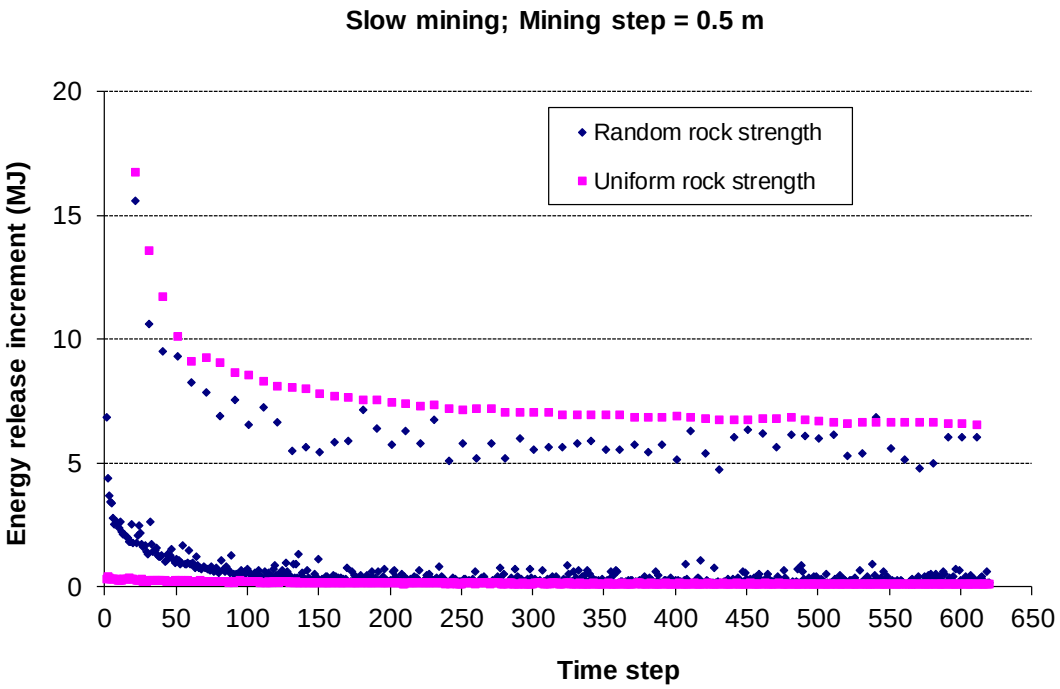

Fig. 15. Comparison between the energy release increments in each mining step when random rock strength and uniform rock strength properties are used. (Slow mining rate with face advance increment = 0.5 m; schedule 3.)

6. Conclusions

A detailed analysis of a simplified time-dependent fracture zone model has been presented. An analytical model of the fracture zone length evolution is presented that provides some insight into the characteristic behaviour of the proposed model. This analysis is used to develop a novel partial fracture algorithm to avoid spurious mesh dependent deformations in the evolving fracture zone region. The implementation of this algorithm in conjunction with a recently developed fast marching method to solve the reef-parallel confining stress distribution in the limit strength model is outlined.

Initial simulation runs have demonstrated that short face advance steps can provide a useful strategy to improve the mining face stability in the extraction of highly stressed regions. This has already been implemented in the South African gold mines for many years based on empirical evidence, but could never be quantified. Further evaluation of this possibility is required. Random rock strength properties yield characteristically different distributions of simulated energy release increments when compared to the assumption of uniform rock strength properties. This is a fruitful research avenue to pursue in understanding the actual seismic trends associated with real mining observations. The proposed model can be used to address a wide variety of practical tabular layout design problems including the investigation of stope face preconditioning blasting and determining remnant pillar extraction strategies.

Future work will include the extended implementation of a partial mined element scheme to allow for the evaluation of small face advance increments without having to resort to very small element sizes which can result in long run times. Additional attention is required as well to broaden the simulation technique to include slip on geological structures and possible simulation of multiple interacting mining horizons. Further work to calibrate the model parameters is also planned.

Acknowledgements-We wish to acknowledge Harmony Gold Mining Company and the Harmony Chair in Rock Mechanics at the University of Pretoria for supporting development of the time-dependent mining rate model.

References

1. Cook NGW, Hoek E, Pretorius JPG, Ortlepp WD and Salamon MDG. Rock Mechanics Applied to the Study of Rockbursts, *J.S. Afr. Inst. Min. Metall*., 966; 66: 435-528.

2. Malan DF. Time-dependent behaviour of deep level tabular excavations in hard rock. *Rock Mech. Rock Engng*., 1999; 32: 2: 123-155,.

3. Napier JAL, Malan DF. A viscoplastic discontinuum model of time dependent fracture and seismicity effects in brittle rock. *Int. J. Rock Mech. Min. Sci. & Geomech. Abstr*, 1997; 34: 1075-1089.

4. Linkov AM. Rockbursts and the instability of rock masses - Schlumberger Award Lecture, *Int. J. Rock Mech. Min. Sci. & Geomech. Abstr*, 1996; 33: 727-732.

5. Nawrocki PA. One-dimensional semi-analytical solution for time-dependent behaviour of a seam. *Int. J. Num. Anal. Meth. Geomech*., 1995; 19: 59-74.

6. Hackett P. An elastic analysis of rock movements caused by mining. *Trans Inst Min Engrs*. 1959; 118:421-435.

7. Berry DS. An elastic treatment of ground movement due to mining – I. Isotropic ground. *J Mech Phys Solids.* 1960; 8:280-292.

8. Berry DS, Sales TW. An elastic treatment of ground movement due to mining – III. Three dimensional problem, transversely isotropic ground. *J Mech Phys Solids.*1962; 10: 73-83.

9. Crouch SL, Starfield AM. *Boundary element methods in solid mechanics*. George Allen & Unwin;1983.

10. Salamon MDG. Elastic analysis of displacements and stresses induced by mining of seam or reef deposits – I. Fundamental principles and basic solutions as derived from idealized models. *J S Afr Inst Min Metall*. 1963; 63: 128-149.

11. Adams GR, Jager AJ. Petroscopic observations of rock fracturing. *J S Afr Inst Min Metall.* 1980; 80; 204-209.

12. Malan DF. A viscoelastic approach to the modelling of the transient closure behaviour of tabular excavations after blasting. *J S Afr Inst Min Metall.* 1995; 95:211-220.

13. Malan DF, Napier JAL, Janse van Rensburg AL. Stope deformation measurements as a diagnostic measure of rock behaviour: a decade of research. *J S Afr Inst Min Metall.* 2007; 107:743-765.

14. Napier JAL, Malan DF. A simplified model of local fracture processes to investigate the structural stability and design of large-scale tabular mine layouts. In: Proceedings of the 48th US Rock mechanics/ Geomechanics Symposium, Minneapolis, 2014.

15. Barron K. An analytical approach to the design of coal pillars. *CIM Bulletin*. 1984; 77:37-44.

16. Barron K, Pen Y. A revised model for coal pillars. In: Proceedings of the Workshop on Coal Pillar Mechanics and Design. Pittsburgh, PA: US Department of the Interior, Bureau of Mines, IC 9315. 1992: 144-157.

17. Brummer RK. Modelling the non-linear behaviour of fractured seams in deep gold mines. In: Proceedings of the Twentieth International Symposium on the Applications of Computers and Mathematics in the Mineral Industries – Volume 1: Mining, SAIMM. Johannesburg, 1987: 21-32.

18. Salamon MDG. Strength and stability of coal pillars. In: Proceedings of the Workshop on Coal Pillar Mechanics and Design. Pittsburgh, PA: US Department of the Interior, Bureau of Mines, IC 9315. 1992: 94-121.

19. Malan DF, Napier JAL. Reassessing continuous stope closure data using a limit equilibrium displacement discontinuity model. *J S Afr Inst Min Metall*. 2018; 118: 227-234.

20. Salamon MDG. Elastic analysis of displacements and stresses induced by mining of seam or reef deposits – II. Practical methods of determining displacements, strain and stress components from a given mining geometry. *J S Afr Inst Min Metall.* 1964; 64: 197-218.

21. Deist FH, Georgiadis E, Moris JPE. Computer applications in rock mechanics. *J S Afr Inst Min Metall.* 1972; 72: 265-272.

22. Ryder JA, Napier JAL. Error analysis and design of a large-scale tabular mining stress analyser. In: Fifth International Conference on Numerical Methods in Geomechanics. Nagoya. 1985: 1549-1555.

23. Napier JAL, Malan DF. The computational analysis of shallow depth tabular mining problems. *J S Afr Inst Min Metall*. 2007; 107:725-742.

24. Peirce AP, Spottiswoode S, Napier JAL. The spectral boundary element method: A new window on boundary elements in rock mechanics. *Int J Rock Mech Min Sci*. 1992; 29: 379-400.

25. Spottiswoode S, Drummond M. Pillar behaviour and seismicity in platinum mines. *J S Afr Inst Min Metall.* 2014; 114: 801-809.

26. Napier JAL. Application of a fast marching method to model the development of the fracture zone at the edges of tabular mine excavations. In: Proceedings of the 50th US Rock mechanics/ Geomechanics Symposium, Houston, 2016.

27. An industry guide to methods of ameliorating the hazards of rockfalls and rockbursts, Chamber of Mines Research Organisation, Chamber of Mines of South Africa, 1988

28. Jager AJ, Ryder JA. A handbook on rock engineering practice for tabular hard rock mines, SIMRAC, Johannesburg, 1999.